


## Bursting on a vortex tube with initial axial core-size perturbations

Lingbo Ji and Wim M. Van Rees <sup>\*</sup>*Department of Mechanical Engineering, Massachusetts Institute of Technology,  
Cambridge, Massachusetts 02139, USA*

(Received 27 November 2021; accepted 29 March 2022; published 21 April 2022)

We simulate and analyze the evolution of a rectilinear vortex tube with initial axial core-size perturbations at circulation-based Reynolds number of 5000. The initial variations in the core size are associated with axial gradients in the azimuthal velocity, which generates azimuthal vorticity. This azimuthal vorticity propagates as twist waves in the axial direction. Varying the initial core-size ratio  $A$  shows that the propagation speed of the twist waves varies linearly with  $A$  and approaches linear stability results of the long-wave limit of Kelvin waves on rectilinear vortex tubes as  $A \rightarrow 1$ . The simulations show that when two twist waves of opposite handedness meet the core expands radially, forming a pair of local ringlike structures with opposite-signed azimuthal vorticity through a process termed vortex bursting. An analysis of the vorticity dynamics during bursting reveals that initially the flow behaves qualitatively like a head-on collision of two isolated vortex rings, with the azimuthal vorticity dynamics driving radial growth. During bursting, however, the localized radial expansion of the core is also accompanied by an increase in the radial vorticity component, which ultimately arrests the bursting and reverses the sign of the azimuthal vorticity. Through long-time simulations of the periodic tube, we demonstrate that after the primary bursting event the twist waves reverse their direction and interact again, leading to further bursting events. The evolution of the perturbed tubes is then accompanied by sustained elevated enstrophy levels and thus accelerated energy decay as compared to undisturbed Lamb-Oseen vortices of identical initial circulation and energy. Overall, this work provides the first detailed qualitative and quantitative insights into the mechanisms and evolution of vortex bursting on rectilinear vortex tubes. To further assess the relevance and prevalence of bursting in practical settings, subsequent investigations in the stability and sensitivity of our results to varying Reynolds number, nonrectilinear vortex center lines, and external strain fields are needed.

DOI: [10.1103/PhysRevFluids.7.044704](https://doi.org/10.1103/PhysRevFluids.7.044704)

### I. INTRODUCTION

Vortex tubes dominate flows across many engineering applications and provide building blocks for turbulent free-space and boundary-layer flows. The fundamental processes governing their dynamics are often characterized by nonlinear instabilities such as vortex breakdown [1], topological changes involving vortex reconnection [2–4], and geometrical reconfigurations that arise in helicity dynamics [5,6]. Understanding the mechanisms and time scales governing these phenomena has practical applications such as drag reduction in turbulent boundary layers [7,8], energy dissipation in aircraft wakes [9,10], erosion damage in turbomachinery [11], and mixing in combustion phenomena [12].

---

\*wvanrees@mit.edu

For an isolated rectilinear vortex tube, the dominant instabilities have been identified and analyzed through a mix of reduced-order models, experiments, and direct numerical simulations. Insights going back to Lord Kelvin [13] have demonstrated that rectilinear axisymmetric vortex tubes support stable wave modes that can propagate along the axial direction. Linear stability analyses have provided significantly more information on different features of these waves, such as their instability in the presence of external strain fields [14,15] and axial flows [16]. Amongst the modes, the  $m = 0$  “sausaging” axisymmetric mode is of particular interest within the current context of vortex tubes with initial axial core-size perturbations. This mode was first simulated using direct numerical simulations of the Navier-Stokes equations in Melander and Hussain [17]. They initialized the simulation as a vortex tube with initial finite amplitude sinusoidal core-size perturbations, at circulation-based Reynolds numbers up to 665.2. Using axisymmetry to reduce the Navier-Stokes equations to a coupling between meridional and swirling flow, the results were used to explain the generation, propagation, and evolution of twist waves. Further theoretical context for the twist waves was provided by Arendt *et al.* [18] who solved the initial value problem of an infinitesimal axial core-size perturbation on a Rankine vortex and described the same governing mechanisms as [17]. The effect of external strain fields and shear layers on the evolution of vortices with initial infinitesimal and finite-amplitude core-size perturbation was further investigated using linear stability analyses and numerical simulations in Schoppa *et al.* [19] and Pradeep and Hussain [20].

The phenomenon of vortex bursting was first mentioned in observations of full-scale and experimental aircraft trailing wakes by Tombach [21], Sarpkaya and Daly [22], and Liu [23]. These works demonstrated that vortex tubes would occasionally develop local radial core-size expansions, which were later included and sketched in Fig. 8 of the review article by Spalart [9]. The first simulations that clearly showed vortex bursting were done by Moet *et al.* [24], who numerically evolved a vortex tube with local core-size variations at circulation-based Reynolds numbers up to 10 000 using direct numerical simulations and  $10^7$  using large-eddy simulations. Their work showed not only the generation and propagation of twist waves on such tubes, as in Melander and Hussain [17], but also the drastic radial expansion of the core into swirling ringlike structures associated with vortex bursting. Recently, the richness of the vortical structures during bursting were shown in a visualization of simulation data at circulation-based Reynolds number of 10 000 in [25], which revealed that the bursting structure consists of two closely spaced and interconnected vortex rings of opposite-signed azimuthal vorticity. Finally we note that the work by [26] analyzes the interactions of rectilinear vortices in aircraft wakes and focuses on tracer transport and secondary vortical structures while referring to vortex bursting phenomena; however, here we will restrict ourselves to vortex bursting originating from the interaction of opposite-signed twist waves on isolated vortex tubes, as in [24,25].

Though the visualizations of [24] and [25] provide first insights into the bursting phenomenon, detailed qualitative and quantitative analyses of the mechanisms underlying vortex bursting are still lacking. In particular, there are open questions concerning the practical consequences of vortex bursting in terms of the energy dissipation and possible loss of coherency due to further instabilities and the dependency of the bursting dynamics on the initial perturbation amplitude. To address these questions, in this work we analyze a rectilinear vortex tube at circulation-based Reynolds number of 5000 with a range of initial core-size perturbation amplitudes. We describe our numerical method and initial setup in Sec. II. This section also contains a brief overview of the global flow evolution, setting up our main analysis in three parts. In Sec. III we analyze the twist waves and their propagation speed. The bursting process itself, its underlying physical mechanisms, and their dependency on the initial core-size ratio are addressed in Sec. IV. In Sec. V, we analyze the late-time flow evolution and energy decay of the vortex tube after the primary bursting event, before concluding in Sec. VI.

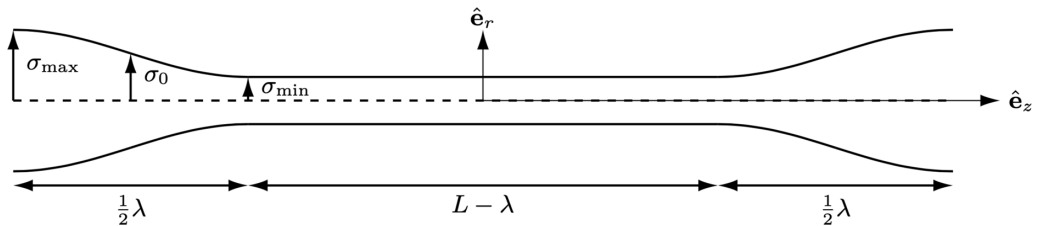


FIG. 1. Sketch of the initial vortex tube within the extent of the computational domain.

## II. NUMERICAL METHOD, SETUP, AND GLOBAL FLOW EVOLUTION

### A. Numerical method

Our simulation method starts from the 3D incompressible Navier-Stokes equations in vorticity-velocity form:

$$\frac{\partial \boldsymbol{\omega}}{\partial t} + (\mathbf{u} \cdot \nabla) \boldsymbol{\omega} = (\boldsymbol{\omega} \cdot \nabla) \mathbf{u} + \nu \nabla^2 \boldsymbol{\omega}, \quad (1)$$

$$\nabla^2 \mathbf{u} = -\nabla \times \boldsymbol{\omega}, \quad (2)$$

where  $\boldsymbol{\omega} = \nabla \times \mathbf{u}$  is the vorticity vector,  $\mathbf{u}$  is the velocity vector, and  $\nu$  is the kinematic viscosity. We use a remeshed vortex method to discretize these equations. In this method, the right-hand side of the vorticity equation is discretized on a regular Cartesian grid using standard finite-difference operators [27,28]. To handle the advection, the method uses a set of Lagrangian particles that are initialized from the grid points at the beginning of each time step and are advected with the flow. The particles' weights are redistributed back onto the grid using a high-order, moment-conserving interpolation kernel at the end of each time step. In this work we use specifically the sixth-order  $M_6^*$  kernel for interpolation between the mesh and particles [29,30], together with fourth-order finite-difference stencils for the stretching and diffusion terms. The Poisson equation for the velocity field is solved using a Fast Fourier Transform, where careful treatment of the Green's function and transformation domain enables the use of arbitrary combinations of free-space and periodic boundary conditions [31,32]. Time integration is done using a fourth-order Runge-Kutta scheme. The time step is controlled through the Lagrangian CFL criterion that sets the time step inversely proportional to the norm of the velocity gradient tensor [30]. To prevent the buildup of discretization errors that could violate the solenoidal nature of the vorticity field, a spectral solenoidal reprojecton is performed every 10 time steps. The solver is implemented in the Parallel Particle-Mesh (PPM) library designed for massively parallel computing [33]. The accuracy of this method has been shown previously by comparing with the pseudospectral methods in [30,34], and the method has successfully been used in a variety of studies on vortical flows [3,6,35].

### B. Setup

All simulations are initialized with an axisymmetric and periodic straight vortex tube with Gaussian core profile. The tube alternates sections of sinusoidal core-size variations with sections that have a constant core radius as illustrated in Fig. 1. Written in cylindrical coordinates  $(r, \theta, z)$ , with  $z$  axis being the center line of the vortex tube, the initially nonzero vorticity components are

$$\omega_r = \frac{r}{\sigma(z)} \frac{d\sigma(z)}{dz} \omega_z, \quad (3)$$

$$\omega_z = \frac{\Gamma_0}{\pi \sigma(z)^2} \exp\left(-\frac{r^2}{\sigma(z)^2}\right), \quad (4)$$

where  $\Gamma_0$  is the circulation of the vortex tube and  $\sigma(z)$  is a function controlling the size of the vortex core.  $\sigma(z)$  is chosen such that the core-size perturbation is of sinusoidal nature, with maximum core size  $\sigma_{\max}$  and minimum core size  $\sigma_{\min}$ . The perturbed regions are separated by a straight segment of length  $L - \lambda$  and core size  $\sigma_{\min}$  (Fig. 1). The initial core-size perturbation is defined in this work by the ratio of the maximum core size to the minimum core size,

$$A = \frac{\sigma_{\max}}{\sigma_{\min}},$$

and the average between the two extreme values of the core size is denoted by  $\sigma_0 = \frac{1}{2}(\sigma_{\max} + \sigma_{\min})$ . The flow field is contained within a rectangular computational domain of size  $\frac{1}{2}L \times \frac{1}{2}L \times L$  with periodic boundary conditions in the  $z$  direction, and unbounded in  $x$  and  $y$  directions [32].

We set  $\sigma_0 = L/20$  and  $\lambda = L - \lambda = 10\sigma_0$ , and consider a range of different initial core-size ratios  $1.286 \leq A \leq 5.4$ . The Reynolds number based on the circulation of the vortex and kinematic viscosity,  $\text{Re}_\Gamma = \frac{\Gamma_0}{\nu}$ , is fixed to be 5000 throughout this work. In the rest of the manuscript,  $t^*$  represents time nondimensionalized with circulation and average core size, i.e.,  $t^* = t \frac{\Gamma_0^2}{\sigma_0}$ .

For simulations of the cases with  $A < 4.333$ , the Cartesian mesh consists of  $384 \times 384 \times 768$  computational elements and, for the cases with  $A \geq 4.333$ ,  $576 \times 576 \times 1152$  computational elements. With these resolutions we ensure a resolution of 16.8–34 grid points across  $\sigma_{\min}$  across the different values of  $A$ . The accuracy of each simulation is verified by comparing the evolution of key flow metrics with that of cases with a lower resolution and ensuring there are no notable differences in the reported results. In addition, we calculate the instantaneous errors in the effective viscosity for each simulation [30], which peaks at 1.6% across all cases. Based on previous experience, this bound is consistent with well-resolved direct numerical simulations [3,30].

### C. Global flow evolution

To frame the analysis and in-depth discussion of the vorticity dynamics below, this section provides a brief overview of the dominant phases in the flow evolution for a representative case with initial core-size ratio  $A = 3.0$ . Figure 2 shows the structure of the vortex tube through the visualization of a set of vortex lines at different times, colored by azimuthal vorticity  $\omega_\theta$ . At  $t^* = 0$  the vortex lines are untwisted and  $\omega_\theta = 0$  everywhere. This initial condition develops twist waves of opposite handedness, as visualized through the opposite-signed azimuthal vorticity  $\omega_\theta$  in Fig. 2. Around  $t^* = 40$  the interaction of the twist waves in the center of the domain leads to the primary vortex bursting event, characterized by a local increase in the core size. Around  $t^* = 80$  the vortical structures are weakened and the directions of azimuthal vorticity in the core are reversed. The opposite-signed twist wave packets travel away from the bursting region before meeting at the periodic boundaries of the domain at around  $t^* = 137.5$ , where a second bursting event occurs.

The global evolution of the vortex tube with initial core-size perturbations can thus roughly be divided into three phases: an early phase of twist wave generation and propagation, the primary bursting event, and the late-time evolution beyond the primary bursting event. In the following sections, we will provide detailed analysis of the features and physical mechanisms in each of these three phases.

## III. TWIST WAVE FORMATION AND PROPAGATION

### A. Twist wave generation and its structure

A vortex tube with initial axial core-size variations is characterized by axial gradients in the azimuthal velocity,  $\partial u_\theta / \partial z$ . This tilts the vorticity vector out of the  $(r, z)$  plane and thus generates regions with nonzero  $\omega_\theta$  components. These bundles of twisted vortex lines have a right handedness (left handedness) if the core size of the vortex tube is converging (diverging) in the direction of positive  $\omega_z$ , as shown in Fig. 2. The twisted regions are well separated by the straight sections of the tube, so that they do not interact; previous works have shown that the purely sinusoidal initial

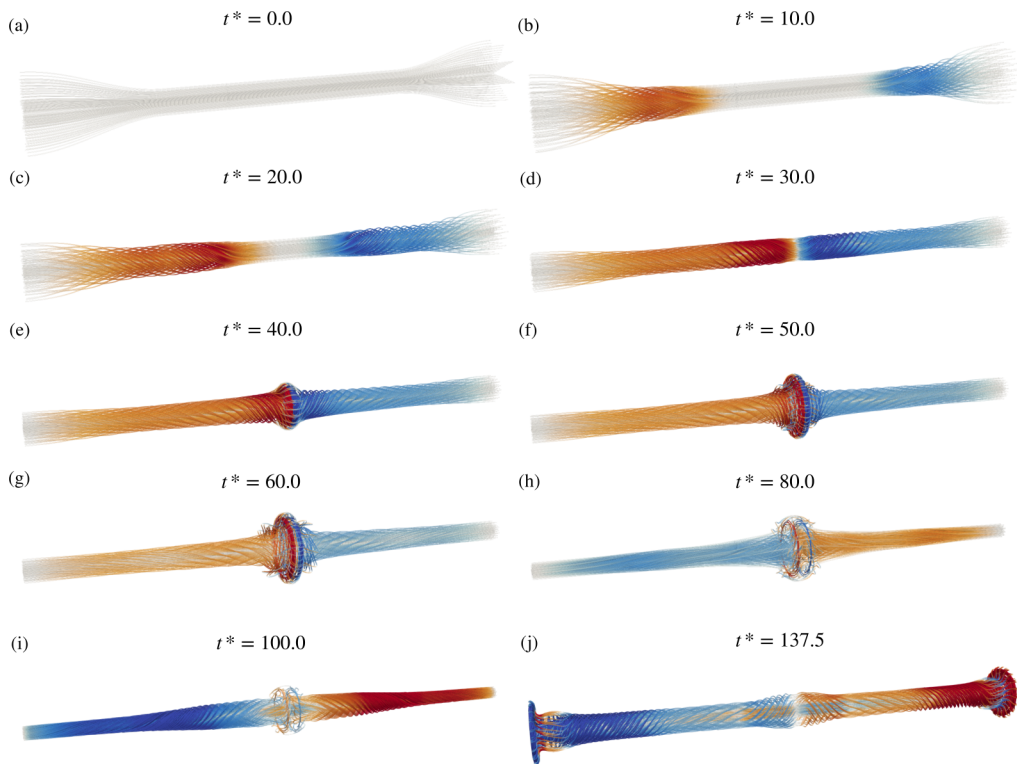


FIG. 2. Visualization of vortex lines colored by azimuthal vorticity  $\omega_\theta$  at different times for the case  $A = 3.0$ . In all cases, the vortex lines are seeded from a disk at the left end of the domain ( $z/\sigma_0 = -10$ ) and their geometry is computed from the instantaneous vorticity vector field.

core-size variations lead to more complex dynamics at early times [17,25]. The evolution of regions of twisted vortex lines on a rectilinear vortex tube has been investigated extensively in previous works using linear stability analyses [18,36] and numerical simulations [17,24]. These studies showed that the associated vorticity field leads to axial velocity variations  $\partial u_z / \partial z$  that feed back into changes in core-size perturbations and differential rotation. The combined effect of these dynamics leads to axial propagation of twist waves [17,18]. In our configuration, the opposite-signed twist waves propagate towards the center of the domain as seen in Fig. 2.

To analyze the structure of the vorticity field inside the twist waves, we examine the twist density defined as  $\tau(r, z) = \frac{\omega_\theta}{r\omega_z}$ . The twist density measures the azimuthal angle turned by a vortex line about the  $z$  axis per unit distance in the axial direction and is thus a natural geometric measure of the degree of twisting of a vortex line [37]. More explanation on the definition and interpretation of this quantity can be found in Supplemental Material Appendix A [38–40]. Figure 3 shows the contours of  $\tau(r, z)$  of the positive-signed twist wave for the case  $A = 3.0$ , at four times in the early flow evolution. The contours show a clear wave front associated with maximum twist density on the center line. Behind, we observe a conical shell-like structure that indicates a radial decay in the axial velocity  $u_z$ . This radial structure of the twist density is seen more clearly in Fig. 4(a), which plots the radial distribution of  $\tau$  at a fixed axial station  $z/\sigma_0 = -2.5$  as the wave travels through this plane. Before the twist wave front reaches this position, the twist density increases from zero to a Gaussian-like profile centered around  $r = 0$ , whose maximum quickly increases as the twist wave front arrives. As the twist wave passes, the peak of the twist profile moves in the radial direction away from the axis and its maximum value decreases.

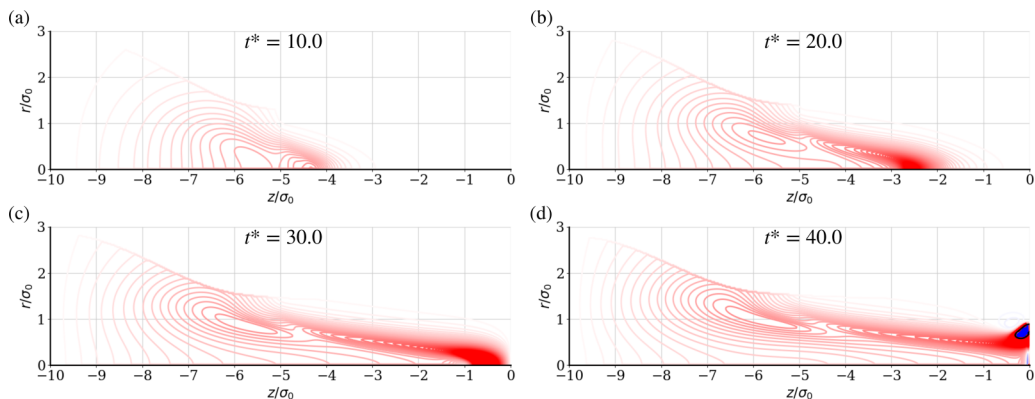


FIG. 3. Twist density  $\tau = \frac{\omega_\theta}{r\omega_z}$  contours in the  $(r, z)$  plane for the case  $A = 3.0$ , showing only the region  $z < 0$ . Red and blue colors correspond to positive and negative values of  $\tau$ , respectively. We set the twist field manually to zero when  $|\omega/(\Gamma_0/\sigma_0^2)| < 0.0026$ , to prevent spurious contours arising from the numerical division of two small numbers.

### B. Twist wave propagation speed

Figure 4(b) shows the twist density profile along the center line at different times for  $A = 3.0$ . This center line twist density shows a clear peak associated with the front of the twist wave, moving axially at an approximately constant speed. The associated wave speed can be quantified through a linear fit of the position of the peak center line twist density over time. By repeating this calculation across all simulations we find that the propagation speed depends linearly on the initial core-size ratio  $A$ , as shown in Fig. 4(c). A linear fit through this data leads to the expression  $c/(\Gamma_0/\sigma_0) \approx 0.0620(A - 1) + 0.0616$ . We note that this is not the only way to track the propagation speed; other metrics for identifying the twist wave front are explained in Supplemental Material Appendix B [38–40], but they all give similar relationships between wave speed and  $A$ .

In the limit of  $A \rightarrow 1$ , the linear fit result gives an estimate of 0.0616 for the wave speed when the core-size perturbation is infinitesimal. This value can be compared with linear stability analyses on axisymmetric core-size perturbations on rectilinear vortex tubes [18,36,41]. These stability analyses describe the generation and propagation of axisymmetric ( $m = 0$ , with  $m$  the azimuthal wave number) Kelvin waves. For an inviscid Rankine vortex tube with a localized infinitesimal

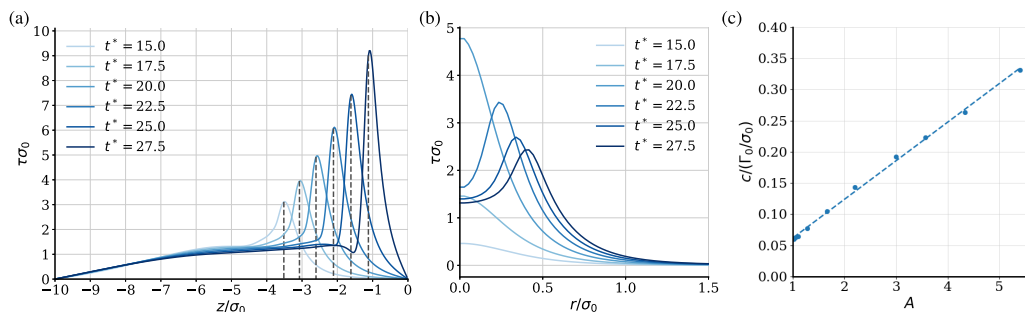


FIG. 4. (a) Radial profile of twist density at different times at  $z/\sigma_0 = -2.5$ . (b) The distribution of twist density  $\tau$  at center line  $r = 0$  at different times for the case  $A = 3.0$ . The dark gray dashed lines denote the positions of the maximum value of  $\tau$ , defined as the wave fronts. (c) The wave speed calculated by tracking the position of the peak value of  $\tau$  along the center line, as a function of the initial core-size ratio  $A$ .



perturbation of a Gaussian shape in the axial direction, Ref. [18] has solved the evolution of the vorticity field over time. We utilize their expressions to numerically evaluate the position of maximum twist density at the center line as a function of time. It is found that the location of maximum twist density reaches a constant speed of  $c/(\Gamma_0/\sigma_0) \approx 0.117$ . Using a different metric to identify the wave front, such as the minimum value in  $\omega_z$  along the center line, gives a similar number. This speed is close to the speed of the long wave ( $k \rightarrow 0$ ) limit of the first radial mode  $n = 1$  of  $m = 0$  Kelvin wave on a Rankine vortex [ $c/(\Gamma_0/\sigma_0) \approx 1/(\pi j_{0,1}) \approx 0.1324$ , where  $j_{0,1}$  is the first zero of the Bessel function of the first kind  $J_0$ ] [42], since this is the fastest traveling wave. A similar analysis for the Lamb-Oseen core profile [36,41] found that the speed in the long wave limit has a value  $c/(\Gamma_0/\sigma_0) \approx 0.1003$  for  $\text{Re}_\Gamma = 2\pi \times 1000$ . This is close to the  $A \rightarrow 1$  values in our fit, with differences possibly explained through the profile of our perturbation and the finite time duration used for our fit.

For finite core-size perturbations  $A > 1$ , our fit can be compared to results in [24], who simulated a long vortex tube with a single isolated core-size perturbation at  $\text{Re}_\Gamma = 10^4$  for  $1 \lesssim A \leq 2$ . They defined  $c$  as the propagation speed of the point of minimum pressure along the center line and also observed that the twist waves propagate at approximately constant speed. A fit of their data using similar normalizations as employed here also leads to a linear relationship between propagation speed and  $A$ , described by  $c/(\Gamma_0/\sigma_0) \approx 0.0241(A - 1) + 0.0918$ . Taking the limit  $A \rightarrow 1$  of the fit based on their data leads to a very close correspondence to the wave speed of 0.1003 from Fabre [41]. We believe that the difference in the fit parameters between Moet *et al.* [24] and our results can be explained by the fact that in the current study the twist waves only propagate for a short time before they interact and bursting occurs. The simulations in Moet *et al.* [24] on the other hand contained a single twist wave propagating over a long distance. We therefore believe that the results in Moet *et al.* [24] capture the theoretical long-wave limit more accurately, hence the favorable comparison with the linear stability results.

To corroborate the linear relationship between twist wave propagation speed and core-size ratio, we briefly discuss a theoretical work related to this topic. In [43], a nonlinear radially averaged inviscid wave model suggests a nontrivial, nonlinear relationship between wave speed and  $A$  for the case of a vortex tube formed by two straight sections of core-size ratio  $1 \lesssim A \leq 5.4$ , under assumptions further detailed in Supplemental Material Appendix C [38]. However, the nonlinearity manifests itself only weakly within this range of  $A$  so that the actual nonlinear relationship is still very well captured by a linear fit.

In summary, numerical and theoretical results suggest that the relationship between nondimensional propagation speed and initial core-size perturbation is well described by a linear fit, whose value as  $A \rightarrow 1$  can be interpreted as the speed of the long wave ( $k \rightarrow 0$ ) limit of the fastest-moving radial mode of a  $m = 0$  Kelvin wave. The precise interpretation of the slope parameter, and the theoretical foundation of the linear fit in general, remains open for future work and could well depend on various subtle features related to core profile and the shape of the disturbance.

#### IV. PRIMARY BURSTING EVENT

When the two twist wave packets of opposite signs collide, vortex bursting occurs. As shown in Fig. 2, for  $A = 3.0$  the characteristic structures during bursting consist of two closely spaced ringlike structures of opposite-signed azimuthal vorticity. These structures form, grow in radius, and eventually decay, while remaining interconnected to each other and the vortex tube as a whole. In this section we analyze this bursting process in detail and determine its qualitative and quantitative dependency on the initial core-size ratio  $A$ .

##### A. Structure of the vorticity field during bursting

The basic structure of the vorticity field for the case  $A = 3.0$  is visualized in Fig. 5 through vortex lines colored by azimuthal vorticity at three different stages of bursting. The top figure shows

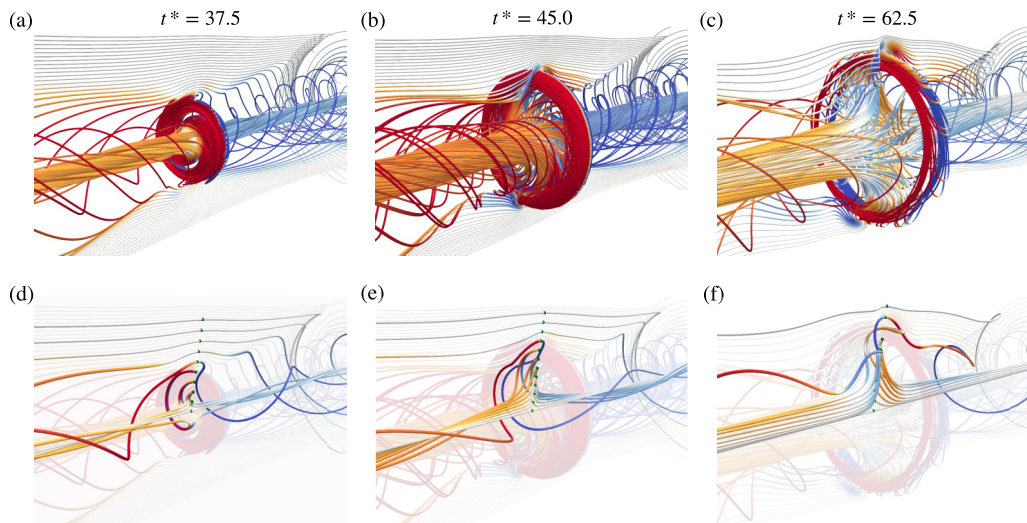


FIG. 5. Bursting process for the case  $A = 3.0$ , visualized within a subdomain centered around the bursting region. (a)–(c) Vortex lines seeded from selected positions and colored by azimuthal vorticity at different stages of bursting. Red and blue colors indicate positive and negative values, respectively. (d)–(f) A reduced version of figures (a)–(c), where the bulk of the vortex lines are visible in the background but only a select set of vortex lines, seeded from a rake at  $z = 0$ , are fully rendered. The seeds for the latter lines are shown by green dots.

an entire bundle of the vortex lines, whereas the bottom figure highlights a few select lines seeded from different radial positions on the center plane.

At  $t^* = 37.5$  the twisted inner core of the tube fans out radially at the center plane, forming a ringlike structure characterized by intense azimuthal vorticity. Topologically the lines remain connected through their mirror images across the center plane, as shown in the bottom view. The vortex lines at large radial distances compared to the core size remain relatively undisturbed. The bursting structure subsequently grows radially. At  $t^* = 45$ , the innermost vortex lines originating close to the center line of the tube undergo a radial expansion but without a significant further winding around the center line. These lines are characterized by very large curvatures on the center plane. Vortex lines that enter the actual bursting structure from larger initial core radii also undergo a large radial expansion but additionally wind around the center line in a swirling pattern. On the “shoulders” of the vortex ring pair, some vortex lines are twisted in the opposite sense of the bursting structure, indicating the presence of opposite-signed azimuthal vorticity. At even larger radial distances the vortex lines are relatively undisturbed. At  $t^* = 62.5$ , the bursting structure has grown further in the radial direction. Though the vortex line structure remains largely similar to  $t^* = 45.0$ , a noticeable difference is that the azimuthal vorticity in the inner core of the center plane has changed sign, indicating the formation of opposite-signed twist waves.

### B. Bursting vorticity dynamics

To understand the physical mechanisms driving the bursting process, we proceed from two perspectives. First, we consider the evolution of the vorticity field within the bursting center plane as driven by the azimuthal vorticity within the ringlike structures on either side of this plane. Second, we will investigate in more detail the dynamics of the azimuthal vorticity component within the bursting structure itself. The dominant mechanisms are inviscid so that we will ignore viscous effects in this subsection.



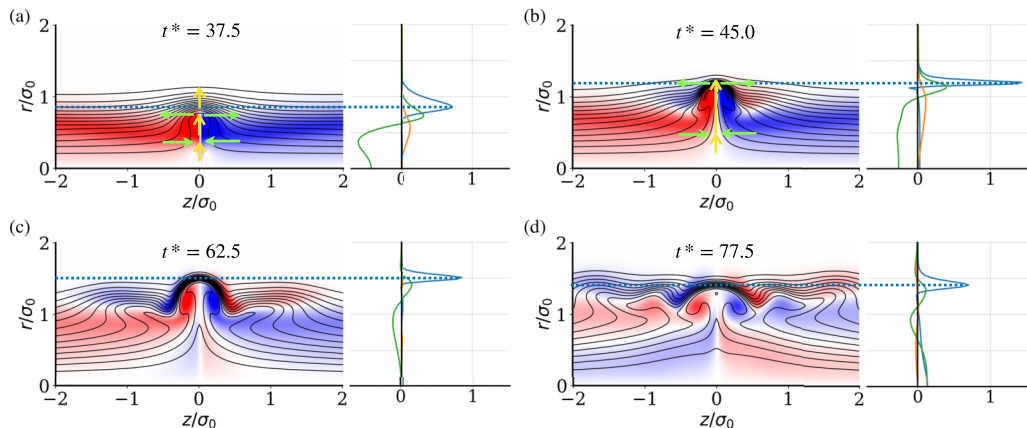


FIG. 6. Visualization of the vorticity field in the  $(r, z)$  plane for  $A = 3.0$  at four different times during bursting. Each subplot shows on the left a filled contour plot of the azimuthal vorticity field in a closeup of the  $(r, z)$  plane around  $z = 0$ , overlaid with black contours of constant  $ru_\theta$  surfaces (vortex surfaces), and on the right the radial profiles at  $z = 0$  of nondimensional axial vorticity  $\omega_z/(\Gamma_0/\sigma_0^2)$  (blue line), radial velocity  $u_r/(\Gamma_0/\sigma_0)$  (orange line), and axial velocity gradient  $\frac{\partial u_z}{\partial z}/(\Gamma_0/\sigma_0^2)$  (green line). In each subplot the vertical radial axes are aligned and the dashed blue line indicates the radial location of the peak value of  $\omega_z$  at  $z = 0$ . In the line plot, the horizontal axis shows the values of the nondimensional quantities on the center plane.

### 1. Center-plane vorticity dynamics

The vorticity field at the center plane  $z = 0$  is, due to symmetry, completely described by  $\omega_z(r, t)$ , which in the absence of viscosity follows the evolution equation

$$\frac{\partial \omega_z}{\partial t} + u_r \frac{\partial \omega_z}{\partial r} = \omega_z \frac{\partial u_z}{\partial z}. \quad (5)$$

The evolution of  $\omega_z$  at the center plane is thus determined by radial advection through  $u_r$  and stretching or compression driven by the axial gradient in  $u_z$ . Both velocity components are completely determined by the azimuthal vorticity on either side of the center plane and related to each other through the solenoidal nature of the velocity field. We plot the radial distribution of  $u_r$ ,  $\partial u_z/\partial z$ , and  $\omega_z$  at the center plane in Fig. 6 at four different times during bursting, for the case  $A = 3.0$ . At  $t^* = 37.5$ , the twist waves have first collided and for small radii ( $r/\sigma_0 \lesssim 1/2$ ) lead to a negative axial gradient of  $u_z$ . This corresponds to an axial compression of the flow and is thus associated with a reduction in  $\omega_z$  on the center plane, as well as a radial expansion of the core ( $u_r > 0$ ). For  $1/2 \lesssim r/\sigma_0 \lesssim 1$ , the azimuthal vorticity on either side of the symmetry plane is associated with a positive axial gradient of  $u_z$ . This gradient of  $u_z$  stretches the axial vorticity and increases its magnitude. As the ringlike bursting structures expand radially, the fundamental features remain in place: a positive  $u_r$  drives the peak  $\omega_z$  radially outwards, axial compression of  $\omega_z$  weakens the vorticity at small radii, and axial stretching intensifies the peak vorticity at large radii.

### 2. Azimuthal vorticity evolution in the bursting region

Though the center plane vorticity explains well the onset of bursting as a function of  $\omega_\theta$ , the evolution of  $\omega_\theta$  itself is of relevance to the later stages of the bursting process. In an axisymmetric field, the time evolution of  $\omega_\theta$  can be written as

$$\frac{D}{Dt} \left( \frac{\omega_\theta}{r} \right) = -2 \frac{u_\theta \omega_r}{r^2} \rightarrow \frac{D\omega_\theta}{Dt} = -2 \frac{u_\theta \omega_r}{r} + \frac{u_r \omega_\theta}{r},$$

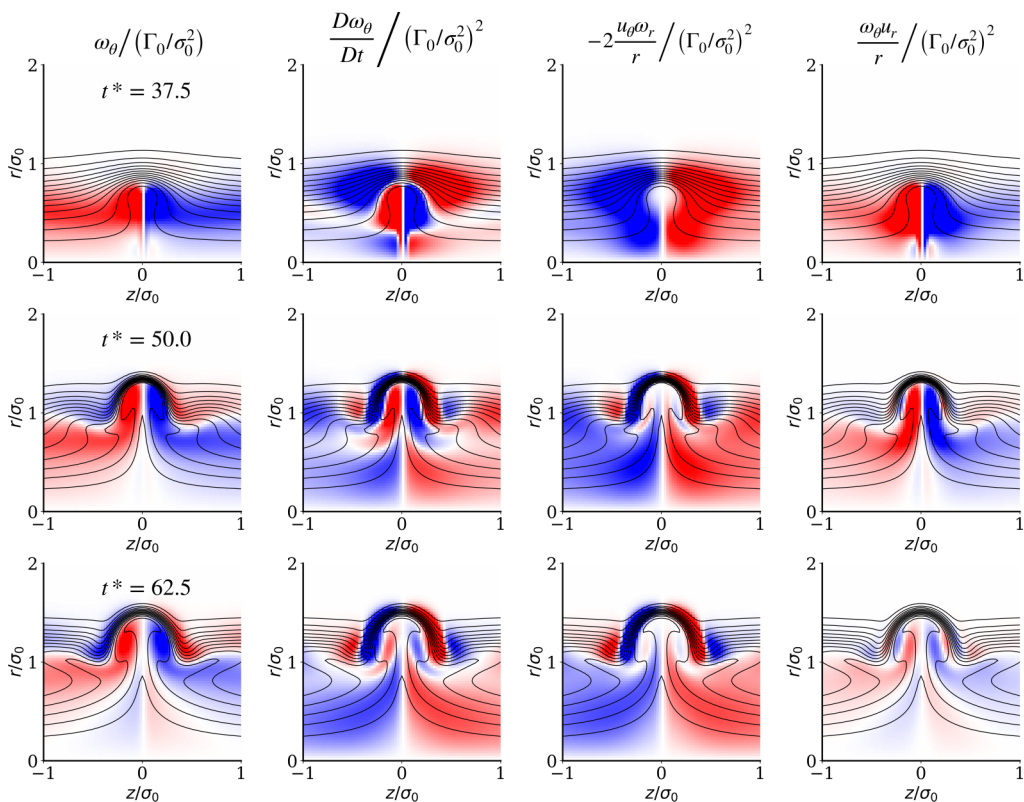


FIG. 7. Contour plots of the different terms in the evolution equation for  $\omega_\theta$  for the case  $A = 3.0$ , overlaid with black contours of constant  $ru_\theta$  surfaces (vortex surfaces). From left to right, we show  $\omega_\theta$ , its total time derivative  $D\omega_\theta/Dt$ , and the two components constituting the total time derivative, namely  $-2\frac{u_\theta\omega_r}{r}$  and  $\frac{u_r\omega_\theta}{r}$ , all in nondimensional form. From top to bottom, we show the fields at three different times during bursting. The color maps for the last three columns are the same.

where  $D/Dt = \partial/\partial t + u_r\partial/\partial r + u_z\partial/\partial z$ . Physically, the first term on the right-hand side  $-2u_\theta\omega_r/r$  relates to the generation of  $\omega_\theta$  through differential rotation induced by an axial gradient in  $u_\theta$  (i.e., tilting) because  $\omega_r = -\partial u_\theta/\partial z$ ; the second term  $\omega_\theta u_r/r$  describes the increase in  $\omega_\theta$  due to stretching associated with  $u_r > 0$ .

Figure 7 examines the interplay between the tilting and stretching terms at different times during bursting for  $A = 3.0$ . The figure shows the relative strength of  $\omega_\theta$  (first column),  $D\omega_\theta/Dt$  (second column), and its two components  $-2u_\theta\omega_r/r$  (third column) and  $\omega_\theta u_r/r$  (rightmost column), all in the meridional plane. At  $t^* = 37.5$ , the sign of  $\omega_\theta$  on either side of the center plane is consistent with the sign of the original twist waves. However, the  $D\omega_\theta/Dt$  field has distinct regions of positive and negative signs. Inside the ringlike bursting structures, the sign of the total right-hand side is consistent with that of  $\omega_\theta$ , indicating that the azimuthal vorticity is intensified. From the rightmost column, we can further see that this is due to the stretching of the vortex lines associated with a positive radial velocity  $u_r$ , as explained in the previous section. However, outside the bursting region the sign of  $D\omega_\theta/Dt$  is opposite to that of  $\omega_\theta$ , due to the tilting of the vortex lines associated with  $\omega_r = -\partial u_\theta/\partial z$ . As a result of these two mechanisms, the field of  $\omega_\theta$  at  $t^* = 50$  contains an intensified azimuthal vorticity within the bursting region and opposite-signed azimuthal vorticity on the shoulders of the structure. As this opposite-signed  $\omega_\theta$  region intensifies, the sign of  $u_r$  above the bursting structure changes from positive to negative, so that the flow compresses radially and

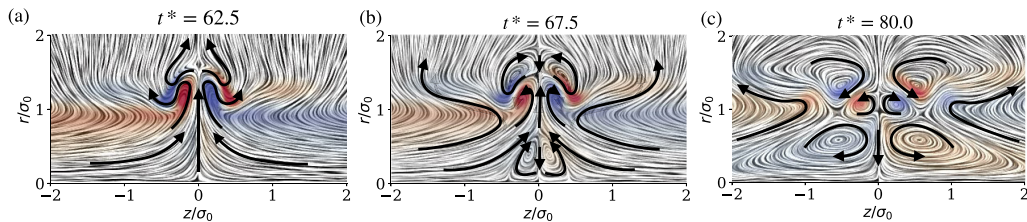


FIG. 8. Velocity field in the  $(r, z)$  plane ( $r > 0$ ) illustrated using line-integral convolution [44], overlaid with colors showing  $\omega_\theta$  at three different times during the late stage of bursting for  $A = 3.0$ . Red and blue indicate positive and negative values of  $\omega_\theta$ , respectively. The black arrows are annotated by hand to indicate the direction of the velocity field.

bursting is arrested. Simultaneously, at radial distances smaller than those of the peak azimuthal vorticity, the  $-2u_\theta\omega_r/r$  term eventually changes the sign of the  $\omega_\theta$  field as on the shoulders.

The evolution at even later times is visualized through a set of images that show the directions of the velocity field in the meridional plane overlaid with the  $\omega_\theta$  field, shown in Fig. 8. The first time in Fig. 8 overlaps with the last time in Fig. 7, which shows the direction of the meridional components of the velocity field associated with the azimuthal vorticity described above. At later times  $t^* = 67.5$  and  $t^* = 80$  we can see the qualitative change in the flow field due to the sign change in  $\omega_\theta$  described above. The velocity  $u_r$  outside the bursting structure has changed sign and is now consistent with a radial compression. Moreover, inside the vortex core the axial velocity is directed away from the bursting region as opposite-signed twist waves are generated and propagate along the axis.

In summary, we can now describe the basic mechanisms of vortex bursting. The azimuthal vorticity from the colliding twist waves compresses the axial vorticity field in the inner core region, leading to expansion of the core radius. Inside the bursting structure this radial expansion initially strengthens the azimuthal vorticity due to stretching. Outside the bursting structure, however, the  $\omega_r$  associated with the core expansion first diminishes and eventually reverses azimuthal vorticity due to vortex tilting. This reversal arrests the growth of the bursting structure and the core relaxes as the newly formed twist waves move away from the bursting plane.

### C. Effect of $A$ on bursting vorticity dynamics

Though the qualitative mechanisms described above for  $A = 3.0$  also dominate the bursting dynamics at other values of the core-size ratio  $A$ , there are some noteworthy qualitative and quantitative differences in the flow evolution that we discuss here.

#### 1. Generation of multiple vortex ring pairs for $A \geq 4.333$

A striking feature of vortex bursting at increasing values of  $A$  is that the growth in azimuthal vorticity associated with the radial expansion of the bursting structure is intensified relative to the strength of the initial  $\omega_\theta$  contained in the twist wave. For  $A \geq 4.333$  this leads to the formation of multiple discrete ringlike pairs: as the early rings rapidly expand outwards due to the growth in  $\omega_\theta$ , they detach from the original twist waves and new rings are being formed behind them. Figures 9(a)–9(c) show this for  $A^* = 4.333$  through the evolution of the azimuthal vorticity. At early time in the bursting evolution, a ringlike pair is generated and expands to a large radius as before. However, around  $t^* = 45$  a second ring pair forms and it merges with the first one around  $t^* = 60$ . When the core-size ratio  $A$  is increased further, more vortex ring pairs are generated successively: in the case of  $A = 5.4$  [shown in Figs. 9(d)–9(i)], at least three vortex ring pairs appear in succession. The occurrence of multiple ringlike structures affects the intensity and duration of bursting, as quantified in the next section.

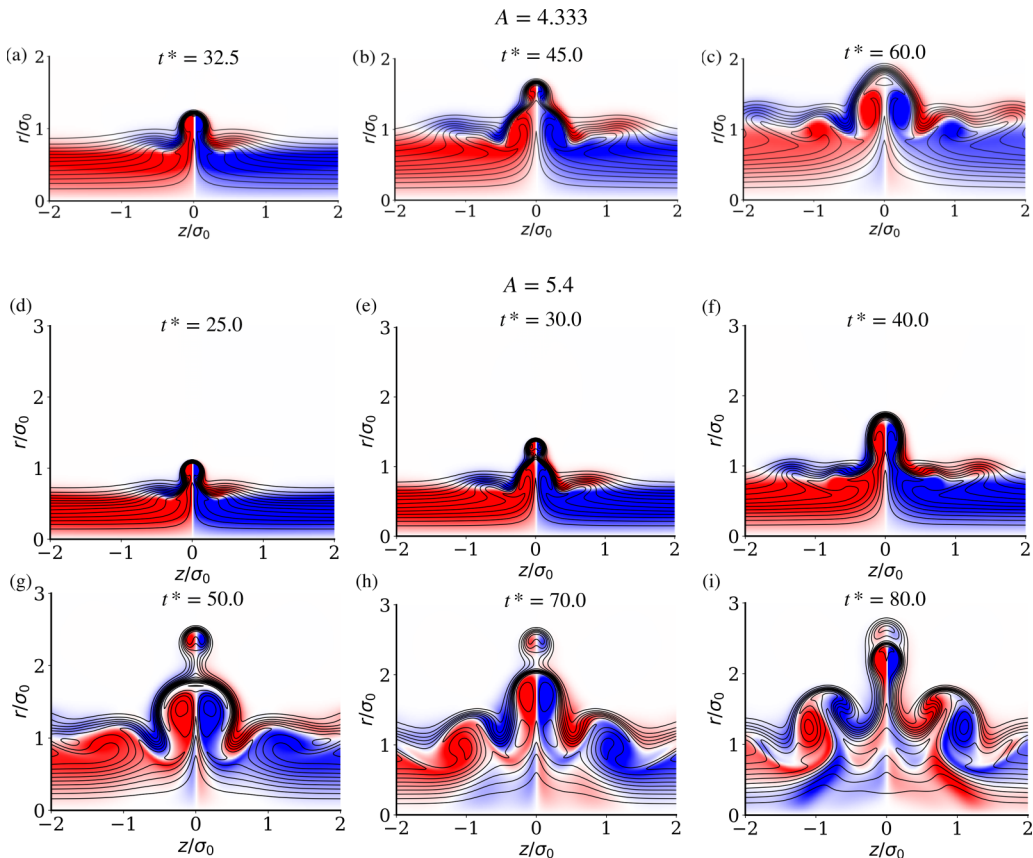


FIG. 9. Visualization of the azimuthal vorticity field in the  $(r, z)$  plane, overlaid with black contours of constant  $ru_\theta$  surfaces (vortex surfaces). The top row shows three different times for  $A = 4.333$  [(a)–(c)], whereas the bottom two rows show six different times for  $A = 5.4$  [(d)–(i)].

## 2. Scaling of time scale and intensity of the bursting event

To provide a quantitative analysis of the bursting process as a function of initial core-size ratio  $A$ , we chose to use the first radial moment of  $\omega_z$ , i.e.,  $I = \int \omega_z r^2 dr / \int \omega_z r dr$ , as a robust metric for measuring the intensity and duration of bursting.

Plotting the evolution of the relative bursting intensity  $I$  as a function of time  $t^*$  [Fig. 10(a)] shows marked differences in the onset and intensity of bursting across the different values of  $A$ . We can account for these differences by defining the start of the bursting event  $t_{\text{start}} = \Delta L/c$ , where  $\Delta L = \frac{L-\lambda}{2} = \frac{L}{4}$  is the distance traveled by each wave packet before collision and  $c$  is the wave speed that we have calculated in Sec. III as a function of the core-size ratio  $A$ . Using the numerically calculated  $I$  values, we can then define  $I_{\text{start}}$  as the value of  $I$  associated with  $t_{\text{start}}^*$ . We further identify for each  $A$  the maximum value of  $I$  as  $I_{\text{max}}$  and denote the nondimensional time when  $I_{\text{max}}$  occurs as  $t_{\text{max}}^*$ . With these quantities we can consider the rescaled bursting intensity  $\hat{I} \equiv \frac{I - I_{\text{start}}}{I_{\text{max}} - I_{\text{start}}}$  and plot this against  $\hat{t} \equiv \frac{t^* - t_{\text{start}}^*}{t_{\text{max}}^* - t_{\text{start}}^*}$ , which follows an almost self-similar profile across all computed values of  $A$  during the buildup stage of the bursting process ( $\hat{t} < 1.0$ ) [Fig. 10(b)]. After the bursting intensity metric  $I$  reaches its maximum during the first bursting ( $\hat{t} = 1$ ), the rescaled profile stays self-similar for  $A \leq 3.571$  for  $\hat{t} \lesssim 1.5$  and deviates afterwards. This deviation can be attributed to differences in radial profile of azimuthal vorticity on either side of the bursting center plane, which determines the relative importance of the different processes governing the reversal of the bursting process, as described

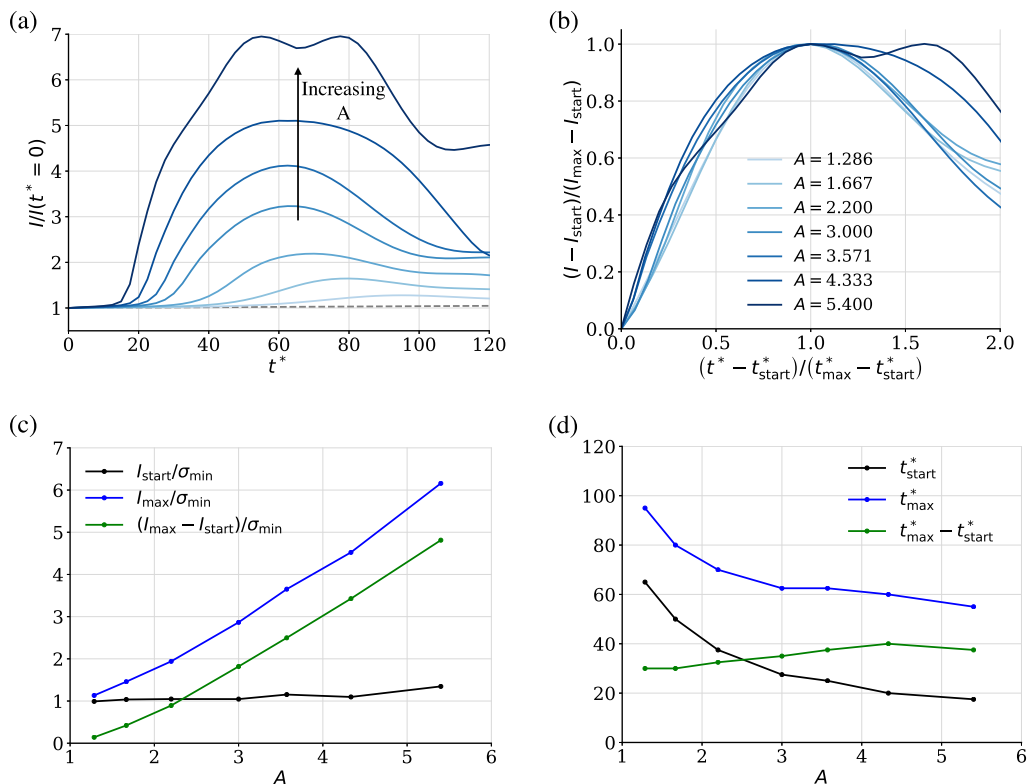


FIG. 10. (a) Time evolution of the first radial moment of  $\omega_z$  at  $z = 0$  ( $I$ ) rescaled by its initial value for different core-size ratios  $A$ . The value of  $A$  increases from 1.286 with lightest blue to 5.4 with darkest blue and the legend is shown in (b). The dashed line denotes the value for  $A = 1$ , i.e., the unperturbed case. (b) The rescaled evolution of  $I$  for different values of  $A$ . (c) The values of  $I$  at  $t_{\text{start}}^*$ ,  $t_{\text{max}}^*$ , and their difference rescaled by  $\sigma_{\text{min}}$  plotted against initial core-size ratio  $A$ . (d) The times associated with the start of bursting, the peak of bursting, and the bursting duration plotted against initial core-size ratio  $A$ .

in the previous section. At the two largest values of  $A$ , the qualitative nature of the lines change as well, associated with the successive generation of multiple vortex ring pairs and their merging.

The intensity of bursting indicated by  $I$  is naturally scaled by the undisturbed radius of the vortex tube at the position of vortex bursting ( $\sigma_{\text{min}}$ ). Figure 10(c) shows that  $I_{\text{start}}/\sigma_{\text{min}} \approx 1$  for all  $A$ , as expected for a metric that measures the onset of bursting. The plot also shows that  $I_{\text{max}}/\sigma_{\text{min}}$  scales roughly linearly with  $A$ . The bursting intensity, as measured by  $(I_{\text{max}} - I_{\text{start}})/\sigma_{\text{min}}$ , thus also increases linearly with the initial core-size ratio. We will see in Sec. VB that this leads to higher enstrophy values and faster energy decay as  $A$  increases. The temporal duration of bursting is quantified by the dependency of  $t_{\text{start}}^*$ ,  $t_{\text{max}}^*$ , and  $t_{\text{max}}^* - t_{\text{start}}^*$  on  $A$ , shown in Fig. 10(d). As explained in Sec. III B,  $t_{\text{start}}^*$  scales as  $A^{-1}$ . The value of  $t_{\text{max}}^*$  also decays with  $A$ , so that the bursting duration  $t_{\text{max}}^* - t_{\text{start}}^*$  only depends weakly on  $A$ . This result needs to be accompanied by two comments. First, as mentioned at the beginning of this work,  $t^*$  is nondimensionalized by  $\Gamma/\sigma_0^2$ , with  $\sigma_0$  the average core size. An alternative nondimensionalization can be formed with  $\Gamma/\sigma_{\text{min}}^2$ , with  $\sigma_{\text{min}} = 2\sigma_0/(A + 1)$  the initial core size of the narrow section of the tube. Using this latter nondimensionalization, the bursting duration would increase roughly quadratically with  $A$ . Second, especially at the higher values of  $A$ , the plot of  $I$  shows a plateau or even a multimodal behavior near its maximum, so that a single time value does not accurately reflect the maximum bursting intensity. Overall, this means that the variation of a single bursting duration metric with  $A$ , as in Fig. 10(d), can only provide a rough indication of the temporal scale of vortex bursting.



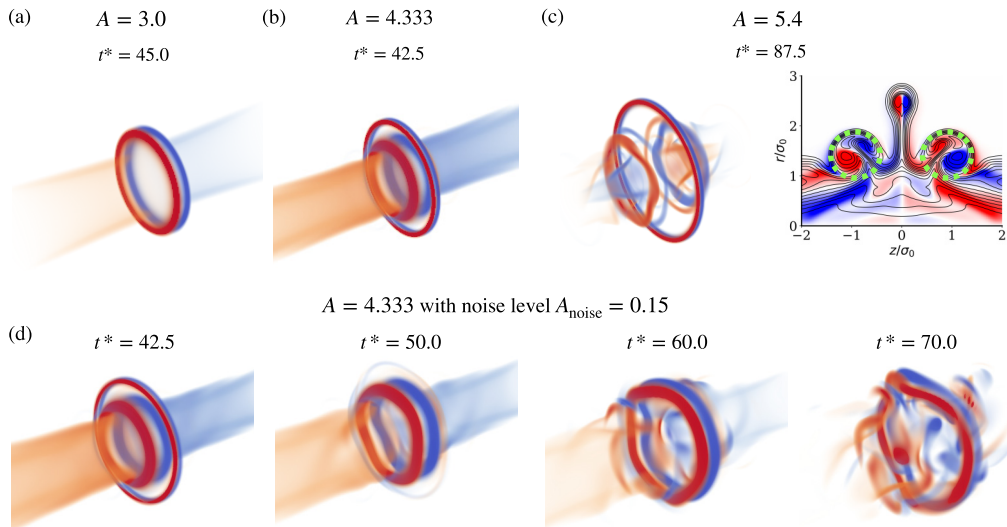


FIG. 11. (a)–(c) 3D volume rendering of the azimuthal vorticity field at selected times during bursting for  $A = 3.0$  (a),  $A = 4.333$  (b), and  $A = 5.4$  (c). The right subfigure of (c) shows the azimuthal vorticity field in the  $(r, z)$  plane for  $A = 5.4$ , with the green dashed circles indicating the side structures where instability develops. The bottom row (d) shows a similar visualization of the 3D azimuthal vorticity field for the case  $A = 4.333$  with nonaxisymmetric noise added to the initial condition.

#### D. Stability of the bursting structure

As mentioned in Sec. IV A above, the early phase of bursting is associated with the radial expansion of two ringlike structures, with dynamics that resemble that head-on collision of two isolated vortex rings [45]. Vortex rings undergoing head-on collisions can be susceptible to instabilities such as the Crow instability [46] and the elliptical instability [15,47], leading eventually to disintegration of the rings [45,48–50]. The onset and details of these instabilities depend on various factors, primarily the effective Reynolds number of the ring, ring thickness (ratio of core radius to ring radius,  $a/R$ ), and the core vorticity distribution [48,50].

In the current study, the effective Reynolds number and thickness of the primary bursting ring pair are estimated by integrating the  $\omega_\theta$  field in the  $(r, z)$  plane within a patch around the maximum value, as detailed in Supplemental Material Appendix D [38]. This analysis shows that the effective Reynolds number of the bursting ringlike pair is in the range  $109 \lesssim \text{Re}_{\text{patch}} \lesssim 379$  (increasing with  $A$ ), with thickness in the range  $0.142 \lesssim a/R \lesssim 0.196$  (decreasing with  $A$ ). This range of Reynolds numbers is well below the threshold of onset of instabilities based on previous simulations of head-on vortex ring collisions [48,50]. Comparing this with our simulation results, when  $A \leq 4.333$  the bursting ring pairs indeed remain stable and axisymmetric during bursting, as shown in Figs. 11(a) and 11(b) for  $A = 3.0$  and  $A = 4.333$ , respectively.

For the case with highest core-size ratio,  $A = 5.4$ , however, an azimuthal instability does occur at a late stage of the primary bursting process, shown in Fig. 11(c). This instability does not appear on the ringlike structures closest to the bursting plane but rather on nonprimary structures that are well-separated from each other. The flow field within these structures, encircled in the right panel of Fig. 11(c), is also characterized by two opposite-signed  $\omega_\theta$  components. One of the components originates from the original twist wave, with the other originating from the tilting effect on the bursting structure shoulders, as discussed above. We observe four waves around the circumference of the nonprimary structures, which are likely triggered by nonaxisymmetric discretization errors in the numerical simulation. To investigate whether the flow at lower  $A$  values also becomes unstable



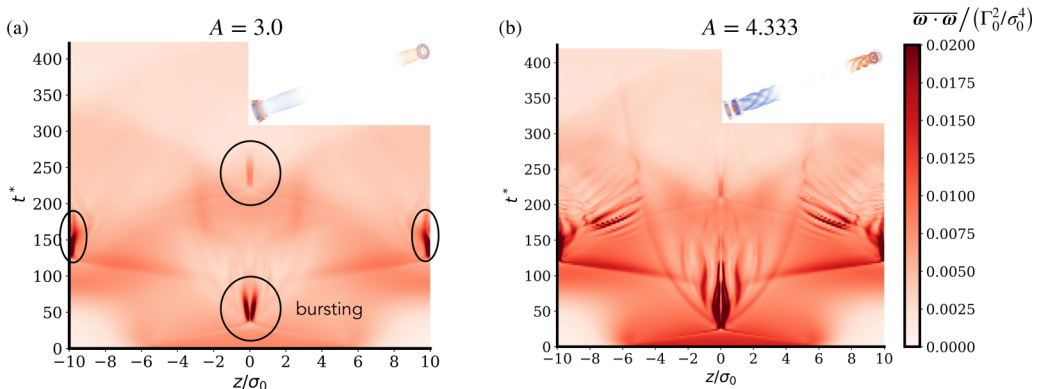


FIG. 12. Plots of radially averaged enstrophy density  $\overline{\boldsymbol{\omega} \cdot \boldsymbol{\omega}} = \frac{\int \boldsymbol{\omega} \cdot \boldsymbol{\omega} dr}{\int r dr}$  as a function of  $z/\sigma_0$  (horizontal axis) and nondimensional time (vertical axis) for  $A = 3.0$  (a) and  $A = 4.333$  (b). The inset figures show 3D azimuthal vorticity field at  $t^* = 160$  for  $A = 3.0$  and for  $A = 4.333$ .

with sufficient noise, we repeated the simulations at  $A = 4.333$  with nonaxisymmetric noise added to the initial condition, as explained in Supplemental Material Appendix E [38]. Figure 11(d) confirms that the late-stage bursting structures become unstable also at  $A = 4.333$  when noise is added, with around four to five azimuthal waves around the circumference of the ring. This indicates that, for sufficiently large  $A$  and/or initial noise, the bursting ring pair can develop azimuthal instabilities despite their low effective Reynolds number.

Two key differences between our results and the head-on collision of two vortex rings can be offered to explain this behavior. First, the ringlike structures during bursting do not evolve in isolation, but rather interact with further vortical structures. These interactions dramatically complicate the flow evolution after the early bursting phase, especially at the larger  $A$  values where instabilities are observed. Second, the bursting ringlike pair is associated with a strong swirling flow due to the existence of nonzero axial vorticity  $\omega_z$  and the two rings are swirling in the same direction. Although detailed studies on the evolution and instability of vortex rings during head-on collision have been carried out in the past [45,48–50], there is little known about the effect of swirl on the flow evolution. Studies on a single isolated vortex ring show that the swirling flow along the vortex ring circumference can suppress azimuthal instability [51], but lead to helical instabilities if the swirling flow is sufficiently large [52]. The combination and relative importance of these two effects on the stability of interacting vortex ring pairs would form useful future research directions to understand the azimuthal instabilities observed in the late stage of bursting at sufficiently large  $A$ .

## V. EVOLUTION BEYOND THE FIRST BURSTING EVENT

The late stage of the primary bursting event leads to the generation of twist waves that travel away from the bursting plane. Due to the axial periodicity of our simulation domain these twist waves interact and further bursting events occur. In this section we discuss two features of the late-time evolution: the appearance of a helical instability at large  $A$  and late times and the global enstrophy evolution and energy decay on vortex tubes where repeated bursting events occur.

### A. Multiple bursting events and helical instability on twist waves

The opposite-signed twist waves generated at the final stages of the first bursting process propagate along the core of the tube and meet, leading to secondary and, for some values of  $A$ , tertiary bursting events at later times. This can be seen in Fig. 12, which shows the space-time evolution of the radially averaged enstrophy  $\overline{\boldsymbol{\omega} \cdot \boldsymbol{\omega}} = \frac{\int \boldsymbol{\omega} \cdot \boldsymbol{\omega} dr}{\int r dr}$  as a function of axial location  $z/\sigma_0$

(horizontally) and time  $t^*$  (vertically) for  $A = 3.0$  (left) and  $A = 4.333$  (right); the same plot for all other values  $A$  is shown in Supplemental Material Appendix F [38].

For  $A = 3.0$ , Fig. 12(a) shows the first bursting event at  $z = 0$  through a spatiotemporally localized increase in enstrophy around  $t^* = 40$ . The secondary bursting event occurs around  $t^* = 125$  at the periodic edges of the domain ( $z/\sigma_0 = \pm 10$ ) and generates further twist waves that cause a tertiary bursting event at  $z = 0$  and  $t^* = 225$ . For the larger initial core-size ratio of  $A = 4.333$ , the plot is initially qualitatively similar, except for small differences around the first bursting event due to the existence of multiple discrete ringlike structures, as discussed in Sec. IV C 1. Beyond  $t^* = 150$ , however, Fig. 12(b) shows distinct streaklike patterns in the radially averaged enstrophy field that are absent at  $A = 3.0$ ; similar patterns are visible for  $A = 5.4$  after the primary bursting event, as shown in Supplemental Material Appendix F [38]. The streaks are associated with the appearance of helical instabilities on the twist waves generated after the respective bursting occurrences, as shown in the inset of Fig. 12(b) and also the animation of the  $\omega_\theta$  field in the Supplemental Material [38]. Such helical instabilities have been analyzed theoretically by [16] in the linear regime and in [24] for isolated twist waves traveling along rectilinear vortex tubes, where their onset was associated with a critical value of the ratio between axial and azimuthal velocity within the tube. Here, however, the helical instability appears to be triggered by vortex bursting, since even at the highest value of  $A$  and with addition of initial noise the associated nonaxisymmetric helical structures never appear before the first bursting occurrence.

After their formation, the helical instabilities sufficiently disrupt the structure of the vortex tube to weaken or fully block further bursting events. This suggests a new pathway for breakup of vortex tubes formed by initial core-size perturbations leading to bursting and bursting leading to helical wave instabilities. The next section quantifies the long-time evolution by examining the evolution of enstrophy and energy compared to an undisturbed vortex tube across the range of  $A$  considered.

### B. Long-time energy and enstrophy evolution

In both cases shown in Fig. 12, the first and second bursting events and the induced vortical structures lead to an elevated level of local enstrophy in the flow and hence an increased energy dissipation rate. This is also seen in the time evolution of total enstrophy and energy plotted in Figs. 13(a) and 13(b), respectively. For all values of  $A$ , the global enstrophy starts a monotonic decay from around  $t^* = 150$ . For the higher values of  $A$ , this decay is associated with the helical instabilities generated on the tube. For the lower values of  $A$  the energy dissipation associated with the earlier bursting events diminishes the intensity of the subsequent bursting occurrences. To characterize the effect of bursting on the late-time energy across all cases, we compare their evolution with unperturbed rectilinear Lamb-Oseen vortex tubes. For each  $A$  we compare with a Lamb-Oseen vortex whose core radius  $\sigma_{\text{ref}}$  is scaled to match the initial energy. The comparison demonstrates that repeated bursting events lead to significantly lower values of energy compared with a reference Lamb-Oseen vortex. To quantify this decay in energy, Fig. 13(c) plots the time it takes for the energy to drop to 95% of its initial value for the perturbed vortices at different values of  $A$ , compared with Lamb-Oseen vortices of the same initial energy. The plot shows that the bursting events lead to a significant acceleration of energy dissipation, with the largest value of  $A$  reaching 95% of its initial energy almost twice as fast as compared with the reference case.

## VI. SUMMARY AND CONCLUSION

This work analyzes the evolution of rectilinear vortex tubes with initial core-size variations at Reynolds number  $\text{Re}_\Gamma = 5000$ , for a range of initial core-size ratios  $1.286 \leq A \leq 5.4$ . We briefly summarize the main contributions below.

(i) In the early phase, the propagation speed of twist waves traveling along the rectilinear axis of the tube is approximately constant in time and can be identified through the position of peak twist density along the center line. The twist wave speed has an approximate linear relationship with  $A$  for

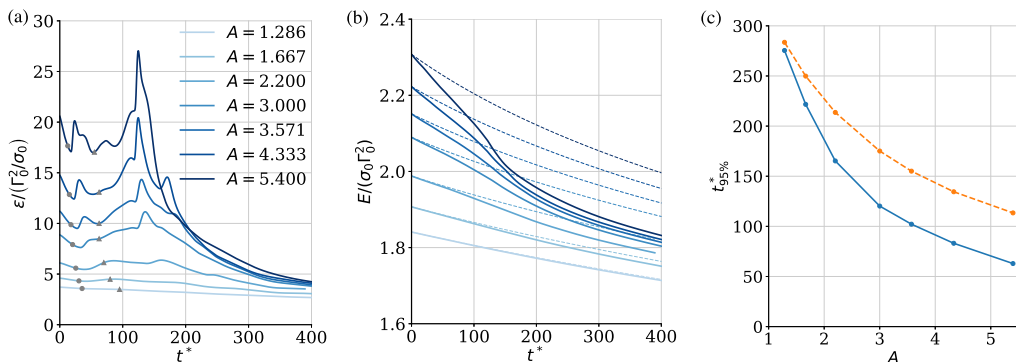


FIG. 13. (a) Time evolution of global enstrophy ( $\varepsilon = \int \boldsymbol{\omega} \cdot \boldsymbol{\omega} dV$ ) for different core-size ratios  $A$ . The gray dots denote the value of enstrophy at  $t_{\text{start}}^*$  and the gray triangles denote the value of enstrophy at  $t_{\text{max}}^*$ , as defined in Sec. IV C 2. (b) The evolution of global energy  $E = 1/2 \int \boldsymbol{\psi} \cdot \boldsymbol{\omega} dV$  for different core-size ratios  $A$ , where  $\boldsymbol{\psi}$  is the stream function. The dashed line represents the evolution of energy for an unperturbed Lamb-Oseen vortex tube whose initial core size is chosen to match the initial total energy for each value of  $A$ . (c) The time it takes for energy to decay to 95% of its initial value as a function of  $A$  for our numerically simulated vortices (solid blue line) compared with Lamb-Oseen vortices with the same initial energy of our simulated vortices at each  $A$  (dashed orange line).

the range of  $A$  considered. When  $A \rightarrow 1$ , the twist wave speed approximates the long wavelength limit found through linear stability analyses of  $m = 0$  Kelvin waves.

(ii) The rapid radial expansion of the vortex core during bursting is driven by the azimuthal vorticity field on either side of the bursting plane. This field itself is initially strengthened as the core expands, predominantly due to stretching as in the head-on collision of two vortex rings. As the core expands, however, the radial component of the vorticity vector increases. This component is negatively proportional to the axial gradient in azimuthal velocity and tilts the vorticity vector. Consequently, the azimuthal vorticity field is weakened and eventually reverses sign, arresting the bursting process.

(iii) Increasing  $A$  increases the intensity of bursting as measured by the radial moment of axial vorticity at the center plane. After rescaling, the early evolution of this radial moment is strongly self-similar across the range of  $A$  considered here.

(iv) For values of  $A$  above  $A \gtrsim 4$ , several discrete ringlike structures are generated during bursting, due to the disparate time scales involved with the original twist wave speed and the radial expansion of the bursting core. The nonprimary ringlike structures are susceptible to non-axisymmetric azimuthal instabilities during the late stages of bursting. We hypothesize that vortical interactions and the strong swirling flow enable these instabilities to form despite the relatively low effective Reynolds number. As the bursting core relaxes and the twist wave direction reverses, the nonaxisymmetric structures trigger helical wave instabilities along the core axis, breaking the coherency of the core and inhibiting subsequent bursting events.

(v) At late times, the periodic nature of the computation domain in the axial direction leads to secondary and tertiary bursting events. Similar to the primary bursting events, these are generally associated with elevated enstrophy levels and thus accelerate the energy dissipation compared to unperturbed rectilinear vortices of the same initial energy and circulation. This is quantified through a comparison with the viscous energy dissipation of a Lamb-Oseen vortex, showing the bursting events drastically reducing the time required for the energy to reach 95% of its initial value.

This work has focused on the effect of  $A$  on the flow evolution, while fixing all other parameters. Out of these other parameters, the effect of the Reynolds number is of particular interest. The main mechanisms we used to understand the bursting mechanics and relaxation are based on inviscid analyses, but we do expect an effect of Reynolds number in several key characteristics. These

characteristics concern the evolution of the bursting dynamics with possible lasting topological changes due to reconnection, the time scale and intensity of the bursting process, the stability of the ringlike structures during bursting at large  $A$ , and the helical wave instabilities observed at later time. Besides the Reynolds number, the relative wavelength of the core size perturbation ( $\lambda/L$ ) is of interest. Examining the limit  $\lambda/L \rightarrow 0$ , corresponding to an isolated bursting phenomenon on an infinitely long tube, would provide a more robust characterization of the twist wave propagation speed; however, this would also require much larger domains to simulate. Further, bursting can occur in other scenarios, such as on vortex loops whose center lines are initially curved and/or characterized by nonzero writhe [6], which brings additional complexity compared to the case considered here. Lastly, it remains to be investigated whether core-size perturbations are the main driver of vortex bursting in practical scenarios, as opposed to the presence of initial twist distributions inside a core of constant radius. Based on our results, however, we believe that vortex bursting is sufficiently robust that it should occur frequently in many practical flows. This work has shown its potential to disrupt the stability of the vortex core and accelerate the energy dissipation in the flow, which merits further investigation into the prevalence of this phenomenon in practical scenarios.

#### ACKNOWLEDGMENTS

This research was supported by the U.S. Army Research Office under Award No. W911NF-21-1-0332.

- 
- [1] S. Leibovich, The structure of vortex breakdown, *Annu. Rev. Fluid Mech.* **10**, 221 (1978).
  - [2] S. Kida and M. Takaoka, Vortex reconnection, *Annu. Rev. Fluid Mech.* **26**, 169 (1994).
  - [3] W. M. van Rees, F. Hussain, and P. Koumoutsakos, Vortex tube reconnection at  $Re_\Gamma = 10^4$ , *Phys. Fluids* **24**, 075105 (2012).
  - [4] J. Yao and F. Hussain, Vortex reconnection and turbulence cascade, *Annu. Rev. Fluid Mech.* **54**, 317 (2022).
  - [5] M. W. Scheeler, D. Kleckner, D. Proment, G. L. Kindlmann, and W. T. M. Irvine, Helicity conservation by flow across scales in reconnecting vortex links and knots, *Proc. Natl. Acad. Sci. USA* **111**, 15350 (2014).
  - [6] M. W. Scheeler, W. M. van Rees, H. Kedia, D. Kleckner, and W. T. M. Irvine, Complete measurement of helicity and its dynamics in vortex tubes, *Science* **357**, 487 (2017).
  - [7] H. Choi, P. Moin, and J. Kim, Active turbulence control for drag reduction in wall-bounded flows, *J. Fluid Mech.* **262**, 75 (1994).
  - [8] J. Kim, Physics and control of wall turbulence for drag reduction, *Philos. Trans. R. Soc. London A* **369**, 1396 (2011).
  - [9] P. R. Spalart, Airplane trailing vortices, *Annu. Rev. Fluid Mech.* **30**, 107 (1998).
  - [10] M. Drela, Power balance in aerodynamic flows, *AIAA J.* **47**, 1761 (2009).
  - [11] A. Hamed, W. C. Tabakoff, and R. Wenglarz, Erosion and deposition in turbomachinery, *J. Propul. Power* **22**, 350 (2006).
  - [12] N. Syred and J. Beér, Combustion in swirling flows: A review, *Combust. Flame* **23**, 143 (1974).
  - [13] W. Thomson, Vibrations of a columnar vortex, *Proc. R. Soc. Edinburgh* **10**, 443 (1880).
  - [14] D. W. Moore and P. G. Saffman, The motion of a vortex filament with axial flow, *Philos. Trans. R. Soc. London, Ser. A: Math. Phys. Sci.* **272**, 403 (1972).
  - [15] C.-Y. Tsai and S. E. Widnall, The stability of short waves on a straight vortex filament in a weak externally imposed strain field, *J. Fluid Mech.* **73**, 721 (1976).
  - [16] E. W. Mayer and K. G. Powell, Viscous and inviscid instabilities of a trailing vortex, *J. Fluid Mech.* **245**, 91 (1992).
  - [17] M. V. Melander and F. Hussain, Core dynamics on a vortex column, *Fluid Dyn. Res.* **13**, 1 (1994).

- [18] S. Arendt, D. C. Fritts, and Ø. Andressean, The initial value problem for Kelvin vortex waves, *J. Fluid Mech.* **344**, 181 (1997).
- [19] W. Schoppa, F. Hussain, and R. W. Metcalfe, A new mechanism of small-scale transition in a plane mixing layer: core dynamics of spanwise vortices, *J. Fluid Mech.* **298**, 23 (1995).
- [20] D. S. Pradeep and F. Hussain, Core dynamics of a strained vortex: instability and transition, *J. Fluid Mech.* **447**, 247 (2001).
- [21] I. Tombach, Observations of atmospheric effects on vortex wake behavior, *J. Aircr.* **10**, 641 (1973).
- [22] T. Sarpkaya and J. J. Daly, Effect of ambient turbulence on trailing vortices, *J. Aircr.* **24**, 399 (1987).
- [23] H.-T. Liu, Effects of ambient turbulence on the decay of a trailing vortex wake, *J. Aircr.* **29**, 255 (1992).
- [24] H. Moet, F. Laporte, G. Chevalier, and T. Poinsot, Wave propagation in vortices and vortex bursting, *Phys. Fluids* **17**, 054109 (2005).
- [25] W. M. van Rees, Vortex bursting, *Phys. Rev. Fluids* **5**, 110504 (2020).
- [26] T. Misaka, F. Holzäpfel, I. Hennemann, T. Gerz, M. Manhart, and F. Schwertfirm, Vortex bursting and tracer transport of a counter-rotating vortex pair, *Phys. Fluids* **24**, 025104 (2012).
- [27] P. Koumoutsakos, Inviscid axisymmetrization of an elliptical vortex, *J. Comput. Phys.* **138**, 821 (1997).
- [28] H. Cottet and P. Koumoutsakos, *Vortex Methods, Theory and Practice* (Cambridge University Press, Cambridge, UK, 2000).
- [29] M. Bergdorf, Multiresolution particle methods for the simulation of growth and flow, Ph.D. thesis, ETH, Zürich, 2007.
- [30] W. M. van Rees, A. Leonard, D. Pullin, and P. Koumoutsakos, A comparison of vortex and pseudo-spectral methods for the simulation of periodic vortical flows at high Reynolds numbers, *J. Comput. Phys.* **230**, 2794 (2011).
- [31] R. W. Hockney and J. W. Eastwood, *Computer Simulation Using Particles* (McGraw-Hill, New York, 1981).
- [32] P. Chatelain and P. Koumoutsakos, A Fourier-based elliptic solver for vortical flows with periodic and unbounded directions, *J. Comput. Phys.* **229**, 2425 (2010).
- [33] I. Sbalzarini, J. Walther, M. Bergdorf, S. Hieber, E. Kotsalis, and P. Koumoutsakos, PPM – a highly efficient parallel particle–mesh library for the simulation of continuum systems, *J. Comput. Phys.* **215**, 566 (2006).
- [34] G.-H. Cottet, B. Michaux, S. Ossia, and G. VanderLinden, A comparison of spectral and vortex methods in three-dimensional incompressible flows, *J. Comput. Phys.* **175**, 702 (2002).
- [35] M. Bergdorf, P. Koumoutsakos, and A. Leonard, Direct numerical simulations of vortex rings at  $Re_\Gamma = 7500$ , *J. Fluid Mech.* **581**, 495 (2007).
- [36] D. Fabre, D. Sipp, and L. Jacquin, Kelvin waves and the singular modes of the Lamb–Oseen vortex, *J. Fluid Mech.* **551**, 235 (2006).
- [37] Note that at the center line of the vortex tube,  $r = 0$  and  $\omega_\theta = 0$ , we determine the twist density through the L'Hôpital rule  $\tau = \frac{1}{\omega_z} \lim_{r \rightarrow 0} \frac{\omega_\theta}{r}$  numerically.
- [38] See Supplemental Material at <http://link.aps.org/supplemental/10.1103/PhysRevFluids.7.044704> for details.
- [39] H. K. Moffatt and R. L. Ricca, Helicity and the Călugăreanu invariant, *Proc. R. Soc. London, Ser. A: Math. Phys. Sci.* **439**, 411 (1992).
- [40] F. B. Fuller, The writhing number of a space curve, *Proc. Natl. Acad. Sci. USA* **68**, 815 (1971).
- [41] D. Fabre, Instabilités et instationnarités dans les tourbillons: Application aux sillages d'avions, Ph.D. thesis, Université Paris VI, Département de mécanique, France, 2002.
- [42] P. G. Saffman, *Vortex Dynamics* (Cambridge University Press, Cambridge, UK, 1993).
- [43] A. Leonard, Nonlocal theory of area-varying waves on axisymmetric vortex tubes, *Phys. Fluids* **6**, 765 (1994).
- [44] B. Cabral and L. C. Leedom, *Imaging Vector Fields Using Line Integral Convolution* (ACM Press, New York, 1993).
- [45] T. T. Lim and T. B. Nickels, Instability and reconnection in the head-on collision of two vortex rings, *Nature (London)* **357**, 225 (1992).
- [46] S. C. Crow, Stability theory for a pair of trailing vortices, *AIAA J.* **8**, 2172 (1970).

- [47] D. W. Moore and P. G. Saffman, The instability of a straight vortex filament in a strain field, [Proc. R. Soc. London, Ser. A: Math. Phys. Sci.](#) **346**, 413 (1975).
- [48] C.-C. Chu, C.-T. Wang, C.-C. Chang, R.-Y. Chang, and W.-T. Chang, Head-on collision of two coaxial vortex rings: experiment and computation, [J. Fluid Mech.](#) **296**, 39 (1995).
- [49] R. McKeown, R. Ostilla-Mónico, A. Pumir, M. P. Brenner, and S. M. Rubinstein, Cascade leading to the emergence of small structures in vortex ring collisions, [Phys. Rev. Fluids](#) **3**, 124702 (2018).
- [50] A. Mishra, A. Pumir, and R. Ostilla-Mónico, Instability and disintegration of vortex rings during head-on collisions and wall interactions, [Phys. Rev. Fluids](#) **6**, 104702 (2021).
- [51] T. Naitoh, N. Okura, T. Gotoh, and Y. Kato, On the evolution of vortex rings with swirl, [Phys. Fluids](#) **26**, 067101 (2014).
- [52] C. Gargan-Shingles, M. Rudman, and K. Ryan, The linear stability of swirling vortex rings, [Phys. Fluids](#) **28**, 114106 (2016).